Ultraweak electron-phonon coupling strength in cubic boron arsenide unveiled by ultrafast dynamics

Z. Y. Tian, Q. Y. Zhang, Y. W. Xiao, G. A. Gamage, F. Tian, S. Yue, V. G. Hadjiev, Jiming Bao, Zhifeng Ren, Erjun Liang, and Jimin Zhao

Ultraweak electron-phonon coupling strength in cubic boron arsenide unveiled by ultrafast dynamics

Z. Y. Tian,[1,2] Q. Y. Zhang,[2] Y. W. Xiao,[2,3] G. A. Gamage,[4,6] F. Tian,[4,6] S. Yue,[5,6] V. G. Hadjiev,[6] Jiming Bao,[5,6,7] Zhifeng Ren,[4,6] Erjun Liang,[1,†] and Jimin Zhao[2,8,9,*]

[1] *School of Physics & Microelectronics, and Key Laboratory of Materials Physics, Zhengzhou University, Zhengzhou 450052, China*

[2] *Beijing National Laboratory for Condensed Matter Physics, Institute of Physics, Chinese Academy of Sciences, Beijing 100190, China*

[3] *School of Physical Science and Technology, ShanghaiTech University, Shanghai 201210, China*

[4] *Department of Physics, University of Houston, Houston, Texas 77204*

[5] *Department of Electrical and Computer Engineering, University of Houston, Houston, Texas,77204*

[6] *Texas Center for Superconductivity at the Univerisity of Houston (TcSUH), University of Houston, Houston, Texas 77204*

[7] *Materials Science & Engineering, University of Houston, Houston, Texas 77204*

[8] *School of Physical Sciences, University of Chinese Academy of Sciences, Beijing 100049, China*

[9] *Songshan Lake Materials Laboratory, Dongguan, Guangdong 523808, China*

* *Corresponding author, Email: jmzhao@iphy.ac.cn*
† *Corresponding author, Email: ejliang@zzu.edu.cn*

We report a time-resolved ultrafast quasiparticle dynamics investigation of cubic boron arsenide (c-BAs), which is a recently discovered highly thermal conducting material. The excited state ultrafast relaxation channels dictated by the electron-phonon coupling (EPC), phonon-phonon scattering, and radiative electron-hole recombination have been unambiguously identified, along with their typical interaction times. Significantly, the EPC strength is obtained from the dynamics, with a value of $\lambda_{T_2} = 0.008$ (corresponding to $\lambda \langle \Omega^2 \rangle = 1.18 \pm 0.08$ ps^{-2}), demonstrating an unusually weak coupling (the smallest EPC strength documented to date) between the electrons and phonons. As a comparison, an ultraweak EPC strength for graphene is also expected. We propose that preserving an ultrasmall EPC strength may be a prerequisite for exhibiting an ultrahigh thermal conductivity. Our investigation provides a new insight for searching and designing ultrahigh thermal conductivity materials. Notably, during our analysis we have generalized the fluence-dependence method for obtaining the EPC strength to room temperature, which can be applied to many other types of quantum materials in the future.

Conventional high thermal conductivity materials mainly include diamond [1,2], graphite [1,3], graphene [4], and hexagonal boron nitride (h-BN) [5]. Both graphene and h-BN only exhibit high thermal conductivity in the *ab* plane, which to some extent limits their application for the next generation electronics devices. In 2013, first-principles calculation results predicted that cubic boron arsenide (c-BAs) has an ultrahigh thermal conductivity [6,7], which was experimentally verified, with an isotropic high thermal conductivity of 1300 $Wm^{-1}K^{-1}$ [8-11]. The high thermal conductivity of c-BAs was attributed to a large gap between its acoustic and optical phonons, which limits the three-phonon scattering rate [10]. To date, investigations have been mainly focused on the phonon-phonon scattering in c-BAs. However, experimental investigation on the EPC of c-BAs or other ultrahigh thermal conductive materials is relatively rarely reported. Here we carry out an ultrafast spectroscopy investigation of a single-crystal c-BAs to directly detect its EPC strength.

Ultrafast time-resolved pump-probe spectroscopy provides a direct way of experimentally obtaining the EPC strength [12-15] in a quantum material. This is achieved through probing the nonequilibrium excited-state photocarrier dynamics. Moreover, it is also an effective means to directly acquire the ultrafast interaction time of other typical couplings between elementary excitations, such as in electron-electron scattering [16] and phonon-phonon scattering [12,13,17,27]. Vast types of condensed matters can be investigated, such as superconductors [12,13,17,18], topological materials [19-26], correlated materials [27-31], two-dimensional materials [32-36], magnetic materials [37,38], as well as semiconductors [39,40]. Thus, ultrafast spectroscopy provides a practical experimental means of discovering and distinguishing the complex interactions and underlying mechanisms behind many novel quantum behaviors—here the unusually small EPC in a high thermal conducting material.

In this work, we directly measure the electron-phonon interaction, phonon-phonon scattering, and electron-hole (e-h) recombination lifetimes in a c-BAs single-crystal under various temperatures, followed by a fluence-dependence investigation of the ultrafast dynamics. Based on these results, we obtain its EPC strength to be $\lambda_{T_2} = 0.008$, which is very small compared with most of the known materials. We also estimate that the EPC strength in graphene is also ultraweak.

Our experimental setup is similar to that reported previously [12,13], in which ultrafast light pulses with 70 fs pulse duration, 250 kHz repetition rate, and 800 nm central wavelength are generated by a laser amplifier. The pump and probe beams are in a near-normal incidence geometry. The wavelength of the pump beam is converted to 400 nm to reduce the interference and an auto-balanced detector is employed to enhance the signal-to-noise ratio. The c-BAs crystal was synthesized using a chemical vapor transport method [9], whose microscopic image is shown in the left inset of Fig. 1(a). It has a zincblende face-centered cubic (fcc) crystal structure in the $F\bar{4}3m$ space group (right inset of Fig. 1(a)). In this experiment, the $1/e^2$ intensity laser spot diameters for the pump and probe beams are 80 μm and 60 μm, respectively. The pump and probe fluences are maintained at 318 μJ/cm^2 and 28.3 μJ/cm^2 in the temperature-dependence experiment, respectively, and the pump fluence varies from 47.8 to 318 μJ/cm^2 in the fluence-dependence experiment.

Figure 1(a) illustrates the ultrafast photoexcited carriers relaxation dynamics of c-BAs at 293 K. The differential reflectivity value $\Delta R/R_0$, which is proportional to the density of photoexcited free carriers [12,13,17,18], rises to a maximum near the so-called time zero (*i.e.*, the time when the pump and probe pulses overlap at the sample surface) and then undergoes an ultrafast relaxation. The signal initially decays quickly, then slowly, and finally reaching a constant value. The ultrafast relaxation kinetics can be fitted by three components of the ultrafast relaxation process, which are shown in Fig. 1(a). The purple, orange, blue dashed curves mark the fast, slow, and slowest components, respectively. The result presented in log-scale is also shown in Fig. 1(b), which clearly demonstrates that the ultrafast process is composed of three relaxation components (marked by three lines), cresponding to the fast, slow, and slowest components. We employ a convoluted exponential-decay function to quantitatively analyze the quasiparticle (QP) dynamics as

$$\Delta R / R_0 = \left[A_{\text{fast}} e^{-t/\tau_{\text{fast}}} + A_{\text{slow}} e^{-t/\tau_{\text{slow}}} + A_0 \right] \otimes \left\{ \frac{1}{\tau_{\text{res}} \sqrt{\pi}} \exp\left[-\left(t / \tau_{\text{res}} \right)^2 \right] \right\}, \tag{1}$$

where A_{fast} and A_{slow} are amplitudes, and τ_{fast} and τ_{slow} denote lifetimes. The slowest component has a lifetime orders of magnitude larger than those of the fast and slow components, which can be described by a constant A_0 (see Appendices). The factor

$\frac{1}{\tau_{res}\sqrt{\pi}}\exp\left[-(t/\tau_{res})^2\right]$ is a Gaussian response function depicting the finite temporal pulse duration. The fitted result is shown as the solid curve in Fig. 1, wich compares well with our experimental data. We verify that, without the third component, the combined fast and slow components cannot fit the data well (see Appendix A).
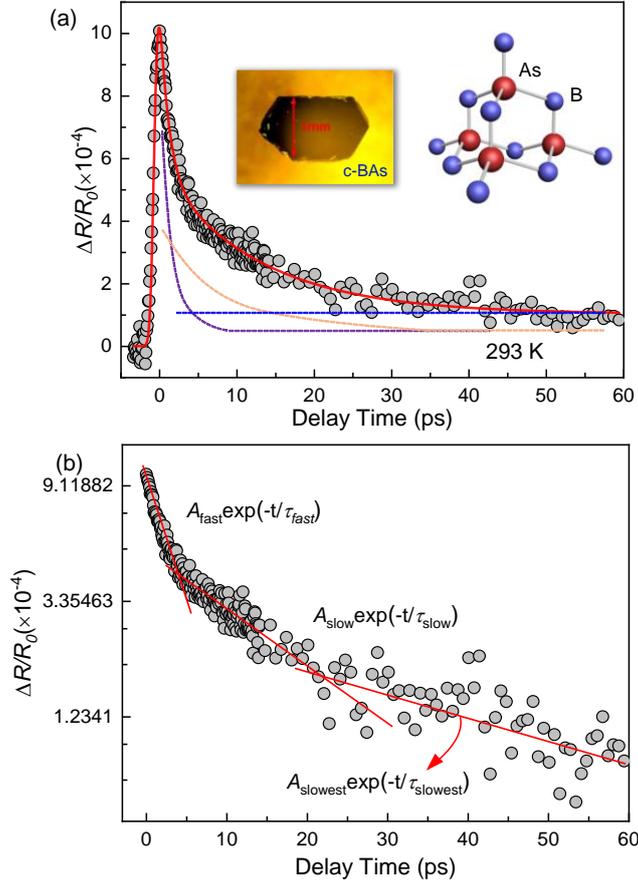
FIG. 1. (a) Ultrafast relaxation of photoexcited carriers in c-BAs at room temperature. Red curve: fitting result according to Eq. (1). Dashed curves: three composing components (purple: fast component, orange: slow component, blue: slowest component). Left inset: photograph of the sample. Right inset: schematic illustration of the lattice structure. (b) Ultrafast relaxation process in the log-scale presentation to reveal the three distinct relaxation channels. Red line: guide to the eyes for the three exponential components, where $A_{slowest}$ and $\tau_{slowest}$ are for the slowest component, with $A_{slowest}$ being identical to A_0 in the text.

The temperature dependence results are shown in Fig. 2. The normalized photoinduced $\Delta R/R_0$ is plotted in Fig. 2(a), which varies prominently and steadily with increasing temperature, without noticeable abrupt change. A colormap of the original $\Delta R/R_0$ data is

displayed in Fig. 2(b), in which warmer tones depict larger $\Delta R/R_0$ values, which is more prominent at low temperatures. The inset to Fig. 2(b) shows the temperature dependence of $|\Delta R/R_0|_{max}$, which exhibits a valley at $T = 100$ K. We note that the static reflectivity R_0 remains constant with varying temperature (see Appendix B). Hence the valley at 100 K, as well as the different behaviors at $T < 100$ K and $T > 100$ K, are not due to R_0. Rather, the slowest component A_0 monotonously decreases with increasing temperature (see Appendix C), and in later paragraph we show that A_{fast} and A_{slow} exhibit different temperature-dependence behaviors. Thus, these factors jointly determine the valley in $|\Delta R/R_0|_{max}$. This is consistant with the absence of reported phase transition around 100 K in this material.
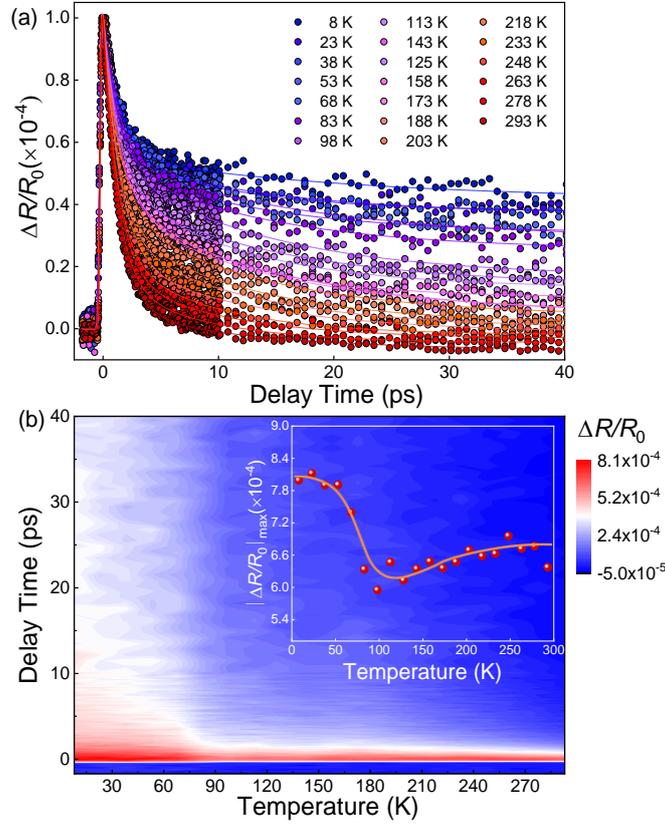
FIG. 2. Temperature-dependence of the ultrafast dynamics. (a) Normalized differential reflectivity at different temperatures. Solid curves: fitting results based on Eq. (1). Note that the time step in the first 10 ps is smaller than that after 10 ps. (b) Two-dimensional color map of the QP dynamics. Inset: temperature dependence of $|\Delta R/R_0|_{max}$. Solid curve: guide for the eyes.

The temperature-dependent fitting parameters A_{fast}, τ_{fast}, A_{slow}, τ_{slow}, and A_0 are summarized in Fig. 3. Both the amplitudes A_{fast} and A_{slow} have a common turning point at 100 K [see Fig. 3(a)]. However, as shown in Fig. 3(b) and 3(c), the lifetimes τ_{fast} and τ_{slow} remain nearly constant over the entire temperature range, except for experimental data fluctuations. Following the convention, we attribute the fast component to the EPC and the slow component to the phonon-phonon scattering [12,13,17,41,42,43]. A brief figure illustration of the different characteristic interaction time scales for various fundamental physical processes can be found in Ref. [41]. Note that here the phonon-phonon scattering is mainly optical phonon to acoustic phonon scattering [39], which is sharply different from the phonon propagation and acoustic phonon to acoustic phonon scattering in various heat diffusion processes. The latter exhibits a much longer characteristic time scale [44,45]. The nearly constant value of τ_{fast} ($\tau_{e\text{-}phonon}$) indicates a constant EPC strength, which is to be expected [12]. In parallel, the relatively constant value of τ_{slow} ($\tau_{phonon\text{-}phonon}$) leads us to predict that c-BAs retains its high thermal conductivity value down to low temperatures, which awaits for future experimental verification.

To elucidate the entire relaxation processes including the constant term A_0, a schematic electronic band structure along the $X\text{-}\Gamma$ direction [46] is shown in Fig. 3(d), along with the inter-band excitation and subsequent intra-band ultrafast relaxation of the photo-excited carriers far above the Fermi level. The pump beam excites electrons from the valence band ground state to the conduction band excited state to produce photo-excited carriers. These photo-excited carriers then exchange energy with the phonons through electron-phonon interactions during the fast relaxtion process. As a result, the photo-excited carriers relax to lower energy states, gradually reaching the bottom of the conduction band and the defect states. During this process, phonon-phonon scattering modulates the electron-phonon scattering, dictating the microscopic quasi-equilibrium between the electrons and phonons [12,13,17,47,48].
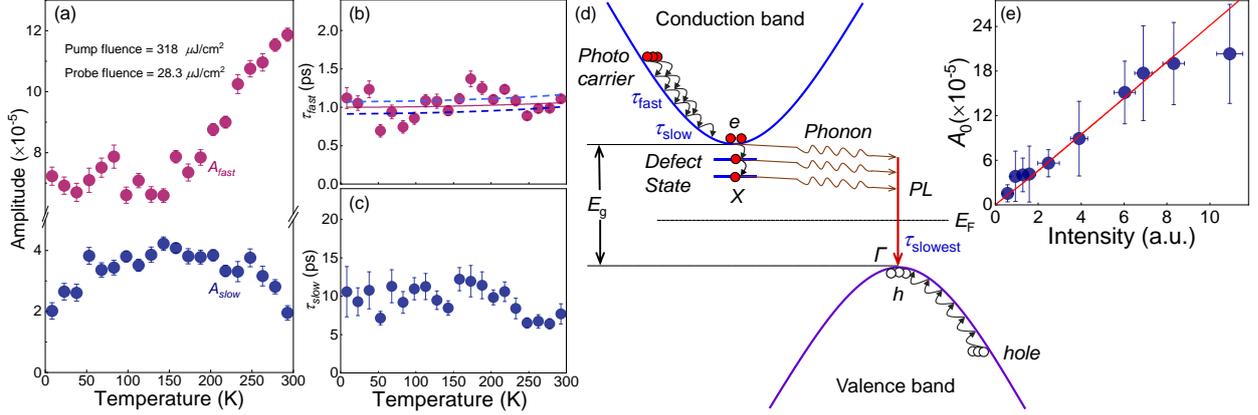
FIG. 3. Temperature dependence of the ultrafast dynamics and the transient relaxation mechanism. (a) Amplitudes A_{fast} and A_{slow}. (b) Lifetime τ_{fast}. Solid curve: fitting result according to Eq. (2). Dashed light and dark blue curves: the fitting curves with maximum and minimum tolerable fitting values of $\lambda \langle \Omega^2 \rangle$, respectively. (c) Lifetime τ_{slow}. (d) Schematic electronic band structure and the multi-process of ultrafast relaxation. The e-h radiative recombination process is also illustrated. (e) Positive correlation between A_0 and the e-h recombination PL intensity at 1.55 eV. Solid line: linear fit of the data.

The slowest component A_0 is attributed to the slow radiative recombination of electrons and holes (e-h). It has been experimentally shown that c-BAs exhibits clear indirect gap photoluminescence (PL) radiation at 1.3-1.8 eV [49] (see Appendix D), which is mainly composed of recombination of free electrons and holes. Our probe beam falls within the energy range of the PL spectra. The photo-excited electrons accumulate at the bottom of the energy bands, and then relax to the defect states; the photo-generated holes also accumulate at the top of the conduction band. These parallel processes are followed by the radiative e-h recombination, which takes much longer time and causes the retardation before the sample resumes its equilibrium state. Apparently, this will lead to a none-zero slowest component, which is clearly detected (Fig. 1(b)). To experimentally unambiguously elucidate this, we explicitly investigate the correlation between the slowest component amplitude A_0 and the PL intensity at 1.55 eV, which is presented in Fig. 3(e). As expected, A_0 exhibits a positive linear correlation to the PL intensity. This is because both quantities decrease with increasing temperature (see Appendix E). Similar slow (phonon-assisted) e-h recombination has also

been observed in a semimetal WTe2 [50]. Because the PL process is an indirect-bandgap transition, it takes a relatively longer time to realize the phonon-assisted e-h recombination; in our experiment, we found that $\tau_{slowest}$ (*i.e.*, $\tau_{e\text{-hole}}$) > 20 ns over the entire temperature range (see Appendix F).

Significantly, we quantitatively investigate the EPC strength by experimental observing τ_{fast}. The EPC strength λ is usually measured under a high fluence regime. It is known [12,14] that in high fluence regime $1/\tau_{fast} = 3\hbar\lambda\langle\Omega^2\rangle / \pi k_B T_e$, where T_e is the temperature of the photo-excited electrons (*i.e.*, electrons at excited states far above the Fermi level), λ is the EPC strength, Ω denotes the phonon frequency, k_B and $\hbar$ are the Boltzman and Planck constants, respectively. From Ref. 12, it is known that $T_e = \left\langle \sqrt{T_L^2 + \dfrac{2(1-R)F}{\kappa_v l_s} e^{-z/l_s}} \right\rangle$, where T_L is the lattice temperature, R is the reflectivity, F is the pump fluence, k_v is the specific heat coefficient [$\kappa_v = \pi^2 N_c N(\varepsilon_F) k_B^2 / 3$, where N_c is the number of cells in the active region and $N(\varepsilon_F)$ is the density of states of both spins per unit cell], l_s is the optical penetration depth, and z is the distance from the sample surface. Thus, to obtain the value of the EPC strength, the reflectivity, specific heat coefficient, and optical penetration depth values are all needed. To date, such values have not been reported for c-BAs. However, this situation can be circumvented by using an approximation and fitting the T_L-dependence results. This is because we detect a series of data points to fit only a few parameters. Making an approximation that the averaging effect in the expression of T_e is equivalent to an effective averaging factor $e^{-z/l_s} \equiv \xi$, for which $0 < \xi < 1$ can be introduced, we have $T_e \approx \sqrt{T_L^2 + \Theta F}$, where $\Theta = 2(1-R)\xi / \kappa_v l_s$. Under the condition of medium and high fluence regimes (*i.e.*, $T_L^2 \ll \Theta F$), we obtain

$$\tau_{fast} = \frac{\pi k_B \sqrt{\Theta F}}{3\hbar\lambda\langle\Omega^2\rangle}(1 + \frac{T_L^2}{2\Theta F}).\tag{2}$$

Eq. (2) extends the well-known relation $1/\tau_{fast} = 3\hbar\lambda\langle\Omega^2\rangle / \pi k_B T_e$ by taking into account that τ_{fast} slightly varies with increasing lattice temperature. Usually this variation is small in many cases. However, by fitting the many data points, one can circumvent the necessity of obtaining the aforementioned physical property parameters when determining the EPC strength. Figure

3(b) shows a well fit of our experimental data by using Eq. (2) (solid curve), which yields an EPC strength of $\lambda\langle\Omega^2\rangle = 1.18 \pm 0.08$ ps^{-2} for our c-BAs sample. Note that the experimental fluctuation (± 0.08 ps^{-2}) is explicitly manifested by two dashed blue curves in Fig. 3(b), which correspond to the maximum and minimum tolerable fitting values of $\lambda\langle\Omega^2\rangle$, respectively. A recent raman spectroscopy of c-BAs [8,10] revealed that the lowest lying optical phonon mode exhibits a frequency of 700 cm^{-1}, which is attributed to a triply degenerate Γ-point phonon mode of T_2 symmetry. It is a transverse optical phonon mode of the B atoms [51]. Thus, the nominal EPC strength λ_{T_2} is obtained to be $\lambda_{T_2} = 0.007 \pm 0.0005$. In a latter paragraph, we explain why we consider a T_2 mode optical phonon in estimating the value of λ.

Furthermore, alternatively, the EPC strength is obtained by measuring the fluence dependence of the dynamics. In our previous work [20], we demonstrated that the fluence-dependence method of obtaining λ is valid for the medium fluence regime. Here, by re-examining its derivation, we make a generalization that it also works well for high fluence regimes. The model in Ref. 20 is for low temperature. In this work, we generalize it to higher temperatures, including room temperature.

Figure 4(a) shows the time-resolved QP relaxation scanning curves at 293 K under various fluences. The inset of Fig. 4(a) shows the fluence dependence of $|\Delta R/R_0|_{max}$, which exhibits a linear relation below 125 μJ/cm^2. This indicates that a slight thermal effect inaugurates when the pump fluence exceeds 125 μJ/cm^2. Note that the definition of medium fluence regime fluctuates with different materials. In our previous study [20], the medium fluence regime was found to be 10 μJ/cm$^2 < F < 1$ mJ/cm^2. In the current investigation of c-BAs, based on the inset to Fig. 4(a), the medium (or medium-high) fluence regime is around 48 μJ/cm$^2 < F < 125$ μJ/cm^2. At $F > 125$ μJ/cm^2, saturation occurs due to the laser heating of the sample, which makes it difficult to go further to the higher fluence regime.
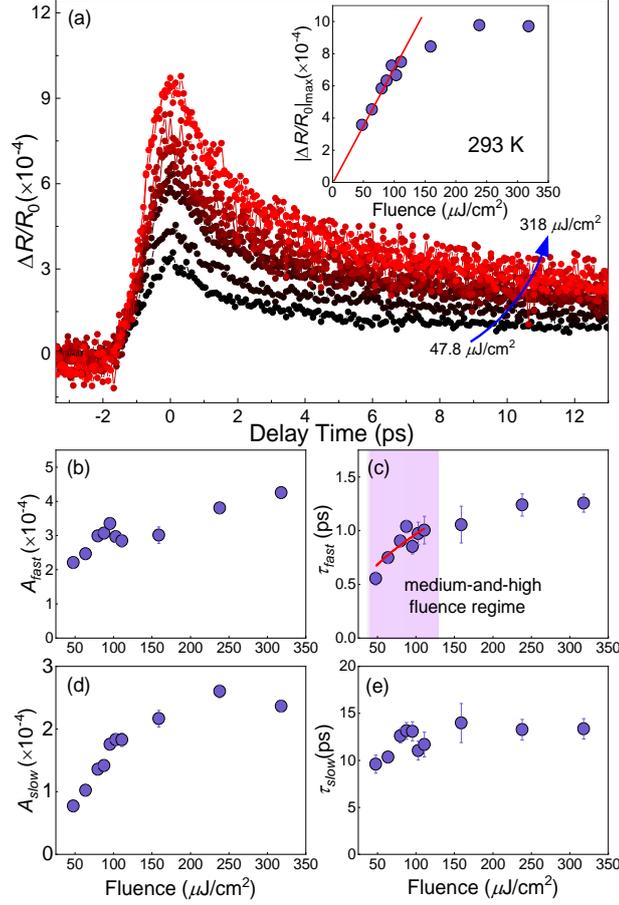
FIG. 4. Pump fluence dependence of the ultrafast QP dynamics at 293 K. (a) The pump fluence increases from 47.8 μJ/cm^2 (black dots) to 318 μJ/cm^2 (red dots). Inset: fluence dependence of $|\Delta R/R_0|_{max}$. Solid line: linear fit of the data. (b-e) Fluence dependence of A_{fast}, τ_{fast}, A_{slow}, and τ_{slow}, respectively. Solid curve: fitting result using Eq. (3). Light purple background: the medium-high fluence regime.

Figures 4(b)-(e) illustrates the fluence dependence values of the fast and slow components, which are obtained by quantitatively analyzing the data using Eq. (1). Both amplitudes A_{fast} and A_{slow} increase with increasing fluence. In Fig. 4(c), the lifetime τ_{fast} exhibits an overall positive correlation with the pump fluence. A light purple background is used to mark the medium-and-high fluence regime.

The enssence of the medium fluence regime method in Ref. 20 is that the second term in $1/\tau_{fast} = 3\hbar\lambda\left\langle\Omega^2\right\rangle/\pi k_B T_e\left[1-\hbar^2\left\langle\Omega^4\right\rangle/12\left\langle\Omega^2\right\rangle k_B^2 T_e T_L+...\right]$ is not omitted, accounting for the relatively not-very-high T_e [14,20]. In Ref. 20, it was derived that

$1/\tau_{\text{fast}} = \dfrac{3\lambda\hbar^2\left\langle\Omega^3\right\rangle}{\pi k_B^2 T_e\left(T_e - T_L\right)}\left[\dfrac{1}{e^{\hbar\langle\Omega\rangle/k_B T_e}-1} - \dfrac{1}{e^{\hbar\langle\Omega\rangle/k_B T_L}-1}\right]$. Because in Ref. 20 $T_L \ll T_e$ and T_e-$T_L \approx T_e$, the

method developed there is only valid for the low temperature case. To extend this equation to

room temperature regime, T_e is replaced with the expression $T_e \approx \sqrt{T_L^2 + \Theta F}$. Thus, we derive

a new relation

$$\tau_{\text{fast}} = \dfrac{\pi k_B^2\sqrt{T_L^2 + \Theta F}\left(\sqrt{T_L^2 + \Theta F} - T_L\right)}{3\lambda\hbar^2\left\langle\Omega^3\right\rangle\left[\dfrac{1}{e^{\hbar\langle\Omega\rangle/(k_B\sqrt{T_L^2+\Theta F})}-1} - \dfrac{1}{e^{\hbar\langle\Omega\rangle/(k_B T_L)}-1}\right]}. \tag{3}$$

In Fig. 4(c), the fitting result using Eq. (3) (solid curve) compares well with our τ_{fast} data,

which yields an EPC strength of $\lambda_{T_2} = 0.008$. This value is very close to the value $\lambda_{T_2} = 0.007$

± 0.0005 obtained above by fitting the T_L-dependence results. The fact that both analysis

treatments yield nearly identical EPC values fortifies the reliability of our data analysis. In

the following, we take $\lambda_{T_2} = 0.008$ as the EPC strength. Figure 4(e) shows that the lifetime

τ_{slow} remains nearly constant, which indicates that the phonon-phonon scattering rate does not

change significantly with increasing pump fluence. It is worth noting that the EPC strength

we have obtained for c-BAs is unusually small. To our knowledge, it is the smallest value for

all the reported materials. For example, among superconductors, the value of λ is usually 10-

500 times larger, ranging from 0.07 to 3.6 [12,13,52-55]. Similarly, the value of λ in Weyl

semimetals [20], carbon nanomaterials [56], two-dimensional materials [57], and

semiconductors [58] is also 1-2 orders of magnitude larger, typically ranging from 0.11 to

0.89 (this is the common values and the exact range must be larger).

In this paragraph, we discuss why we consider a T_2 mode optical phonon in estimating

the value of λ. It is known that acoustic phonons are non-polar and do not couple easily with

electrons. According to [59], in a solid without piezoelectric effect and deformation potential,

the polar coupling between electrons and optical phonons can be very large in ionic crystals.

(Similar to c-BN, c-BAs has ionic crystal characteristics due to the different electronegativity

of the B and As atoms.) Hence, the value $\lambda\left\langle\Omega^2\right\rangle$ is mainly contributed by the optical phonons,

particularly the LO phonons [59]. From the phonon dispersion [51], the LO and TO modes T_2

optical phonons have the smallest values of frequency among all the OP modes. Thus, only

considering the optical phonon modes, we have the average value $\langle\Omega^2\rangle > \langle\Omega_{T_2}^2\rangle \equiv \Omega_{T_2}^2$. From the above, we know $\lambda = \pi k_B T_e / 3\hbar\langle\Omega^2\rangle\tau_{\text{fast}} = C/\langle\Omega^2\rangle$, where τ_{fast} is detected in the experiment, T_e is determined by the sample and laser fluence, and C is a constant for the given experimental condition. If we denote the nominal EPC strength corresponding to the T_2 optical phonon mode as λ_{T_2}, we have $\lambda_{T_2} = C/\langle\Omega_{T_2}^2\rangle \equiv C/\Omega_{T_2}^2 > C/\langle\Omega^2\rangle \equiv \lambda$. Therefore, λ_{T_2} sets the maximum upper limit value for the value of λ (i.e., as a matter of fact, $\lambda < \lambda_{T_2}$). Our investigation results show that even the value of λ_{T_2} is ultrasmall. Thus λ much also be ultrasmall. This means that electrons and phonons couple extremely weakly in c-BAs, being weaker than any reported materials to date.

We contemplate that this unusually small EPC strength is a ubiquitous property for all known similar ultrahigh thermal conductivity materials. Before this work, the EPC strength has not been previously investigated for ultrahigh thermal conducting materials. Here, other than c-BAs, we also examine the pristine graphene, which is a prototypical ultrahigh thermal conductive material with a thermal conductivity of 3000 Wm^{-1}K^{-1} [60]. We carry out an analysis based on the published experimental data to obtain the EPC of graphene. Temperature dependence of ultrafast relaxation of an epitaxial graphene sample on SiC substrate [61], fluence dependence of ultrafast dynamics of a CVD grown graphene sample on glass substrate [62], and room temperature ultrafast dynamics of CVD grown graphene on hBN and glass substrates [63] have been reported. All these works report a fast lifetime of graphene of 0.3~1 ps, which is 0.3~1 times of τ_{fast} for c-BAs. As the substrates are different in these reported works, this range of value may as well applies for a prestine suspended graphene. Mean while, it is well known that the lowest-energy optical phonon mode of graphene is 1591.6 cm^{-1} [62], which is 2.27 times the value for c-BAs. Given these information, even though the detailed experimental data, thermal and optical parameters, and information regarding deconvolusion and data analysis are inaccessible, one can expect that the EPC of graphene is at the same order of (more likely smaller than) that of c-BAs. A smaller EPC value of graphene corresponds to the fact that the thermal conductivity of graphene is higher than that of c-BAs.

Furthermore, we summarize a few well known high thermal conductivity materials in Table. 1. A shared feature is that all these materials exhibit a very high frequency for the lowest-energy optical phonon mode. We contemplate that ultraweak EPC is a crucial universal characteristic for all ultrahigh thermal conducting materials. If it is true, our finding provides an important clue for searching high thermal conducting materials in the future: only those materials with ultraweak EPC strength are likely to preserve ultrahigh thermal conductivity. So far, the mechanism underlying the ultrahigh thermal conductivity of c-BAs has been attributed to the large gap between its optical and acoustic phonons [8-10]. Suppose in a material that has a strong electron-phonon coupling (EPC), it will unlikely occur that pure phonon-phonon scattering dominates the thermal conductivity, because there will be electronic "stickiness" to the phonons (see Appendix G). If phonons in a solid are "dressed" by electrons (manifested as having a significant EPC strength), it is unlikely that this material's thermal conducting mechanism is purely phonon-phonon scattering (see Appendix G). Hence, it is unlikely that the material has a very high thermal conductivity, as compared with those electronic thermal conducting materials. Thus, having an ultrasmall EPC strength may be required for exhibiting an ultrahigh thermal conductivity.

Material	κ (Wm^{-1}K^{-1})	Ω (cm^{-1})	τ_{fast} (ps)	λ_{T_2} or λ_G
Graphene	3000[60]	1592[62]	0.3~1[61-63]	<0.008[this work],*
Diamond	2290[64]	1333[64]	N/A	N/A
c-BAs	1300[8]	700[8,10]	1 [this work]	0.008[this work]
BN	940[6]	1055[65]	N/A	N/A

Table 1. Thermal conductivity κ, frequency of the lowest-energy optical phonon mode Ω, fast component lifetime τ_{fast}, and EPC strength λ of graphene, diamond, c-BAs, and BN. *: estimated to be at the same order to or smaller than that of c-BAs.

In conclusion, we have experimentally obtained the EPC strength for the highly thermally conducting semiconductor c-BAs through the ultrafast time-resolved QP dynamics. We obtain the lifetimes for the electron-phonon interaction, phonon-phonon scattering, and e-h recombination, namely $\tau_{e-phonon} = 1$ ps, $\tau_{phonon-phonon} = 9$ ps, and $\tau_{e-hole} > 20$ ns. We also predict that the high thermal conductivity remains down to low temperatures. Significantly, we obtain

the EPC strength $\lambda_{T_2} = 0.008$ (corresponding to $\lambda\langle\Omega^2\rangle = 1.18 \pm 0.08$ ps^{-2}) for c-BAs, which is smaller than all known reported values. We further estimate the EPC value for graphene is at the same order or smaller than that of c-BAs, which reveals a potential shared feature for ultrahigh thermal conducting materials. In addition, we have generalized the medium fluence regime method of obtaining λ from low to room temperature, which is essential for a broad range of quantum materials.

APPENDIX A: FITTING RESULTS OF THE EXPERIMENTAL DATA

To distinctly observe the component composition of experimental data, we employed different component functions to fit the experimental data. Figure 5 illustrates the three-component and two-component functions fitting results. The fitting result (red curve in Fig. 1) from three-component function (Eq. 1) compares well with our experimental data, but the two-component function (blue curve in Fig. 5) does not.
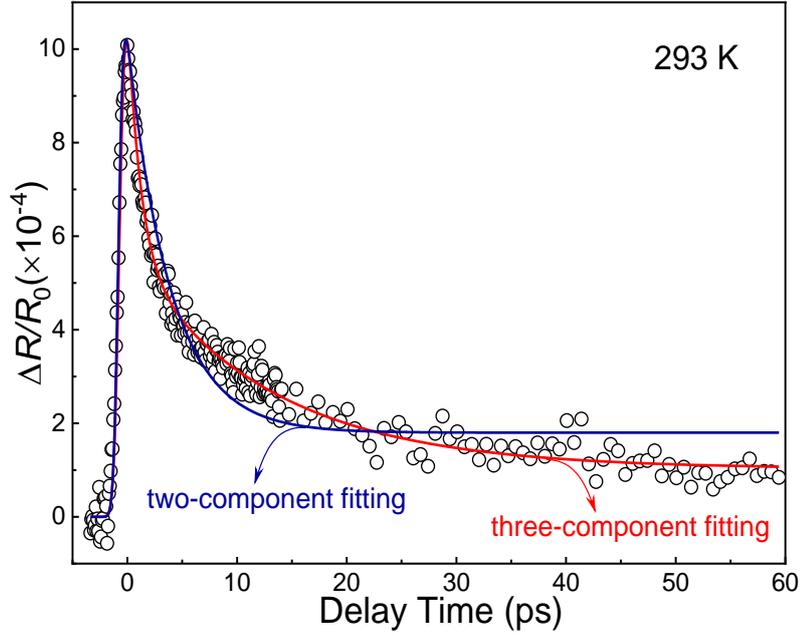
FIG. 5. Ultrafast QP relaxation processes of c-BAs at room temperature. Black circles: experimental data. The three-component (red curve) and two-component (blue curve) functions fitting results.

APPENDIX B: TEMPERATURE DEPENDENCE OF THE STATIC REFLECTIVITY R_0

Experimental data of the static reflectivity R_0 was obtained and is displayed in Fig. 6, which shows that it remains constant with varying temperature.
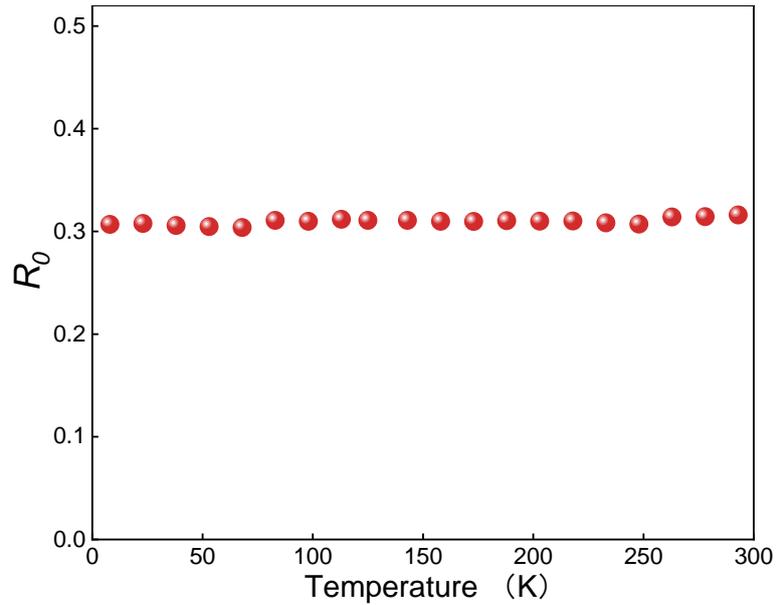
FIG. 6. Temperature dependence of the static reflectivity R_0.

APPENDIX C: TEMPERATRUE DEPENDENCE OF THE SLOWEST COMPONENT A_0

To investigate the temperature dependence of the ultrafast QP relaxation dynamics, the behaviour of the slowest component A_0 was analysed and is displayed in Fig. 7, which shows that it monotonously declines with increasing temperature.
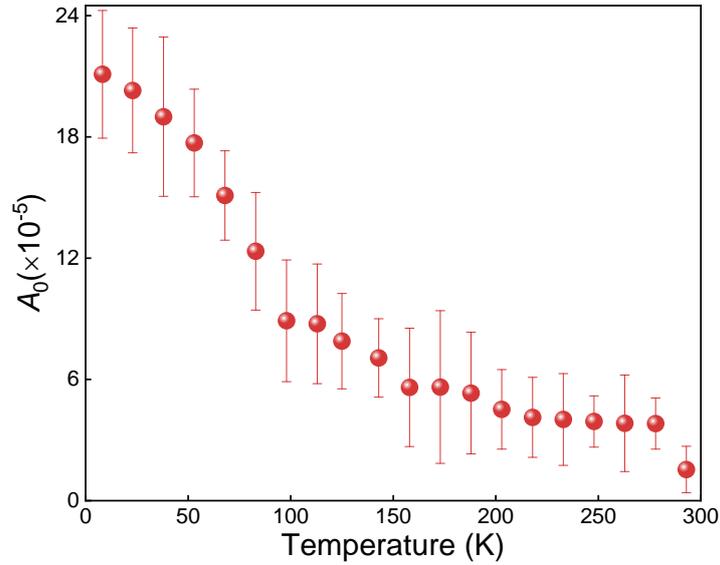
FIG. 7. Temperature-dependence of the slowest component A_0.

APPENDIX D: EVOLUTION OF THE PHOTOLUMINESCENCE (PL) OF c-BAs WITH VARYING TEMPERATURE

The PL spectra [44] decrease in intensity with increasing temperature. The wavelengths of the pump and probe beams are 400 nm and 800 nm, respectively. As a result, the pump photon energy is 3.1 eV, while that of the probe remains 1.55 eV. In Fig. 8, the probe photon energy is indicated by a red dashed line.
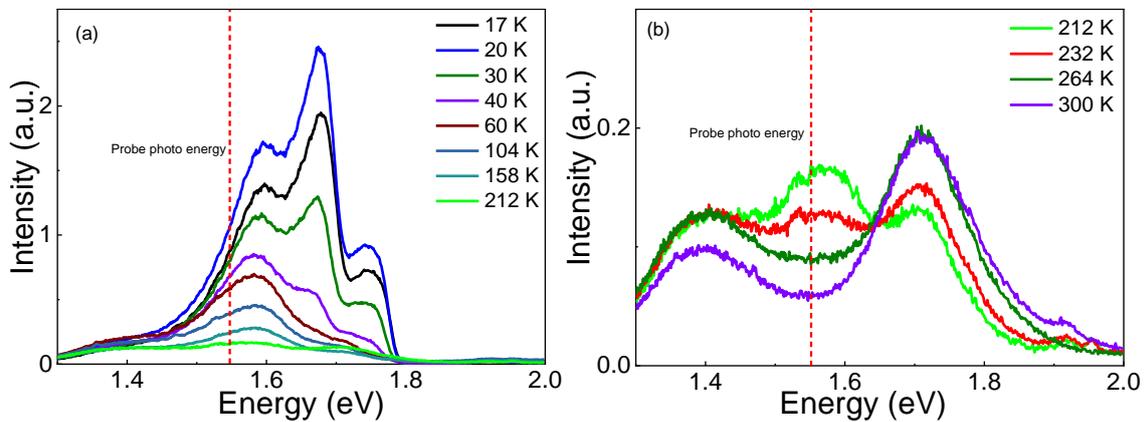
FIG. 8. Evolution of PL of c-BAs as a function of temperature (a) from 17 to 212 K and (b) from 212 to 300 K [44]. Red dashed line: probe photon energy of 1.55 eV. Data adapted from Ref. 44.

APPENDIX E: TEMPERATURE DEPENDENCE OF THE PL INTENSITY AT 1.55 eV

We explicitly investigated the PL intensity with varying temperature at 1.55 eV, and the results are shown in Fig. 9. The PL intensity decreases with increasing temperature, which reflects the thermal excitation of the loosely bound electrons and holes [Ref. 44 in the main text].
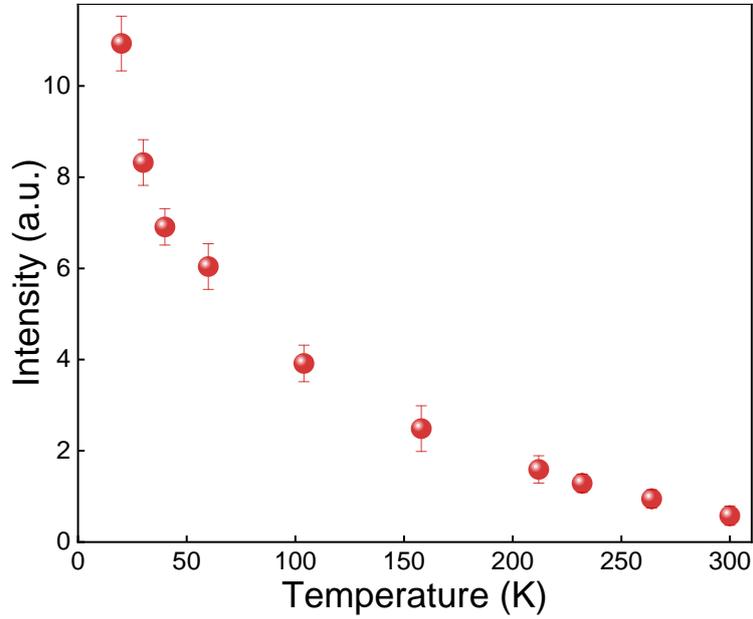
FIG. 9. Temperature dependence of the PL intensity at 1.55 eV. Data adapted from Ref. 44 in the main text.

APPENDIX F: TEMPERATURE DEPENDENCE OF THE LIFETIME $\tau_{slowest}$

In our fitting function Eq. (1) in the main text, the third term A_0 represents the slowest exponential decay component, but since its lifetime is order of magnitude larger than that for A_{fast} and A_{slow}, we use a constant value instead. Thus, Eq. (1) can be rewritten as follows:

$$\Delta R / R_0 = \left[A_{fast} e^{-t/\tau_{fast}} + A_{slow} e^{-t/\tau_{slow}} + A_{slowest} e^{-t/\tau_{slowest}} \right] \otimes \left\{ \frac{1}{\tau_{res} \sqrt{\pi}} \exp\left[-\left(t / \tau_{res} \right)^2 \right] \right\}, \qquad (4)$$

where A_{fast}, A_{slow} and $A_{slowest}$ are the amplitudes and τ_{fast}, τ_{slow}, and $\tau_{slowest}$ denote the lifetimes.

The factor $\frac{1}{\tau_{res}\sqrt{\pi}}\exp\left[-\left(t/\tau_{res}\right)^2\right]$ is a Gaussian response function depicting the finite temporal pulse duration. The temperature-dependent fitting parameter $\tau_{slowest}$ is displayed in Fig. 10, which shows that $\tau_{slowest} > 20$ ns over the entire temperature range. Since the PL process is an indirect-bandgap radiative transition, it takes at least 20 ns to realize the phonon-assisted electron-hole recombination.
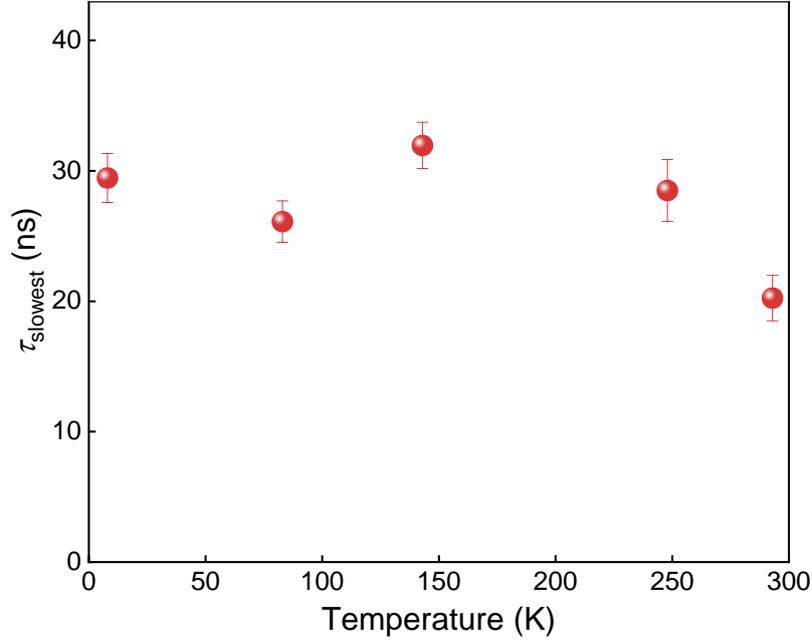
FIG. 10. Temperature dependence of the lifetime $\tau_{slowest}$.

APPENDIX G: SCHEMATIC OF THE ROLE OF EPC IN DETERMINING WHICH THERMAL CONDUCTING MECHANISM OUTWEIGHS IN AN INSULATOR OR SEMICONDUCTOR

As known, there are at least two types of mechanisms for thermal conduction, $\kappa_{tot} = \kappa_e + \kappa_{ph} + \kappa_{other}$ [66]. The final outcome of the dominating mechanism depends on the competition between the two mechanisms. Suppose in an insulator (or semiconductor) that has a strong electron-phonon coupling (EPC), it will unlikely occur that pure phonon-phonon scattering dominates the thermal conductivity, because there will be electronic "stickiness" to the phonons. If phonons are "dressed" by electrons (manifested as having a significant EPC strength), its thermal conductivity will be close to that of the electronic thermal conductivity. Hence, it is unlikely that the material has a very high thermal conductivity (Fig. 11). Such

electron-phonon coupling has been overlooked in previous thermal conductivity investigations.
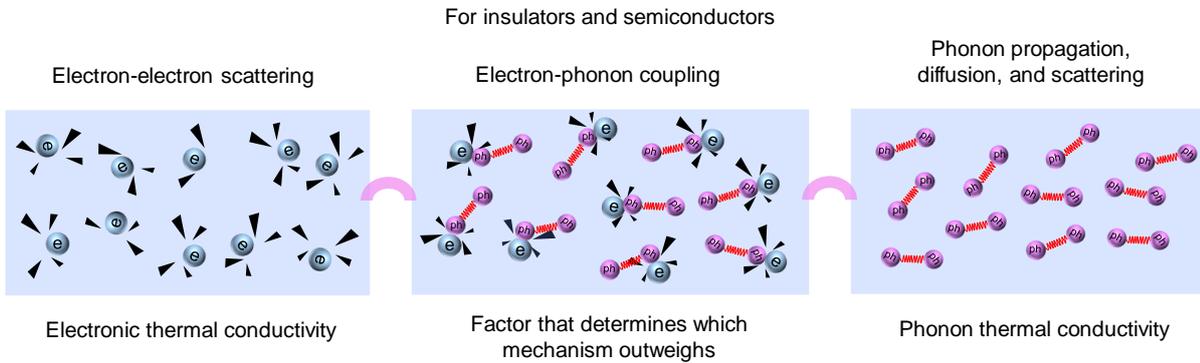
FIG. 11. Schematic role of EPC in determining which thermal conducting mechanism outweighs in an insulator or semiconductor.

References

[1] G. A. Slack, Nonmetallic crystals with high thermal conductivity, J. Phys. Chem. Solids **34**, 321-335 (1973).

[2] L. Wei, P. K. Kuo, R. L. Thomas, and W. F. Banholzer, Thermal Conductivity of Isotopically Modified Single Crystal Diamond, Phys. Rev. Lett. **70**, 3764 (1993).

[3] G. A. Slack, Anisotropic Thermal Conductivity of Pyrolytic Graphite, Phys. Rev. **127**, 694-701 (1962).

[4] S. S. Chen, Q. Z. Wu, C. Mishra, J. Y. Kang, H. J. Zhang, K. Cho, W. W. Cai, A. A. Balandin, and Rodeny S. Ruoff, Thermal conductivity of isotopically modified graphene, Nat. Mater. **11**, 203-207 (2012).

[5] J. C. Zheng, L. Zhang, A. V. Kretinin, S. V. Morozov, Y. B. Wang, T. Wang, X. J. Li, F. Ren, J. Y. Zhang, C. Y. Lu, J. C. Chen, M. Lu, H. Q. Wang, A. K. Geim, and K. S. Novoselov, High thermal conductivity of hexagonal boron nitride laminates, 2D Mater. **3**, 011004 (2016).

[6] L. Lindsay, D. A. Broido, and T. L. Reinecke, First-principles determination of ultrahigh thermal conductivity of boron arsenide: A competitor for diamond, Phys. Rev. Lett. **111**, 025901 (2013).

[7] L. Lindsay, D. A. Broido, and T. L. Reinecke, Phonon-isotope scattering and thermal

conductivity in materials with a large isotope effect: A first-principles study, Phys. Rev. B **88**, 144306 (2013).

[8] J. S. Kang, M. Li, H. Wu, H. Nguyen, and Yongjie Hu, Experimental observation of high thermal conductivity in boron arsenide, Science **361**, 575 (2018).

[9] F. Tian, B. Song, X. Chen, D. Broido, L. Shi, G. Chen, and Z. Ren, Unusual high thermal conductivity in boron arsenide bulk crystals, Science **361**, 582 (2018).

[10] S. Li, Q. Y. Zheng, Y. C. Lv, X. Y. Liu, X. Q. Wang, P. Y. Huang, D. G. Cahill, and B. Lv, High thermal conductivity in cubic boron arsenide crystals, Science **361**, 579 (2018).

[11] G. A. Gamage, K. Chen, G. Chen, F. Tian, and Z. Ren, Effect of nucleation sites on the growth and quality of single-crystal boron arsenide, Materials Today Physics **11**, 100160 (2019).

[12] Q. Wu, H. X. Zhou, Y. L. Wu, L. L. Hu, S. L. Ni, Y. C. Tian, F. Sun, F. Zhou, X. L. Dong, Z. X. Zhao, and Jimin Zhao, Ultrafast quasiparticle dynamics and electron-phonon Coupling in $(Li_{0.84}Fe_{0.16})OHFe_{0.98}Se$, Chin. Phys. Lett. (Express Letter) **37**, 097802 (2020).

[13] Y. C. Tian, W. H. Zhang, F. S. Li, Y. L. Wu, Q. Wu, F. Sun, G. Y. Zhou, L. L. Wang, X. C. Ma, Q-K. Xue, and Jimin Zhao, Ultrafast Dynamics evidence of high temperature superconductivity in single unit cell FeSe on $SrTiO_3$, Phys. Rev. Lett. **116**, 107001 (2016).

[14] P. B. Allen, Theory of Thermal Relaxation of Electrons in Metals, Phys. Rev. Lett. **59**, 1460 (1987).

[15] L. Stojchevska, P. Kusar, T. Mertelj, V. V. Kabanov, X. Lin, G. H. Cao, Z. A. Xu, and D. Mihailovic, Electron-phonon coupling and the charge gap of spin-density wave iron-pnictide materials from quasiparticle relaxation dynamics, Phys. Rev. B **82**, 012505 (2010).

[16] J. Shah, *Ultrafast spectroscopy of semiconductors and semiconductor nanostructures*, Heidelberg: Springer-Verlag Berlin, 1996.

[17] D. H. Torchinsky, G. F. Chen, J. L. Luo, N. L. Wang, and N. Gedik, Band-dependent quasiparticle dynamics in single crystals of the $Ba_{0.6}K_{0.4}Fe_2As_2$ superconductor revealed by pump-probe spectroscopy, Phys. Rev. Lett. **105**, 027005 (2010).

[18] V. V. Kabanov, J. Demsar, B. Podobnik, and D. Mihailovic, Quasiparticle relaxation

dynamics in superconductors with different gap structures: Theory and experiments on YBa$_2$CuO$_{7-\sigma}$, Phys. Rev. B **59**, 1497 (1999).

[19] F. Sun, T. Zhang, C. J. Yi, Y. L.Wu, H. Zhao, Q. Wu, Y. G. Shi, H. M. Weng, and Jimin Zhao, Spin-polarized gap in the magnetic Weyl semimetal Co$_3$Sn$_2$S$_2$, Phys. Rev. B **104**, L100301 (2021).

[20] Q. Wu, F. Sun, Q. Y. Zhang, L. X. Zhao, G. -F. Chen, and Jimin Zhao, Quasiparticle dynamics and electron-phonon coupling in Weyl semimetal TaAs, Phys. Rev. Mater. **4**, 064201 (2020).

[21] F. Sun, Q. Wu, Y. L. Wu, H. Zhao, C. J. Yi, Y. C. Tian, H. W. Liu, Y. G. Shi, H. Ding, X. Dai, P. Richard, and Jimin Zhao, Coherent helix vacancy phonon and its ultrafast dynamics waning in topological Dirac semimetal Cd$_3$As$_2$, Phys. Rev. B **95**, 235108 (2017).

[22] D. Hsieh, F. Mahmood, J. W. Mclver, D. R. Gardner, Y. S. Lee, and N. Gedik, Selective probing of photoinduced charge and spin dynamics in the bulk and surface of a topological insulator, Phys. Rev. Lett. **107**, 077401 (2011).

[23] M. C. Wang, S. Qiao, Z. Jiang, S. N. Luo, and J. Qi, Unraveling photoinduced spin dynamics in the topological insulator Bi$_2$Se$_3$, Phys. Rev. Lett. **116**, 036601 (2016).

[24] B. H. Yu, Z. Y. Tian, F. Sun, D. C. Peets, X. D. Bai, D. L. Feng, and Jimin Zhao, Ultrafast quasiparticle dynamics and coherent phonon in nodal line topological material LaBi, Opt. Express **28**, 383995 (2020).

[25] C. Y. Jiang, F. Sun, Z. L. Feng, S. B. Liu, Y. G. Shi, and Jimin Zhao, Time-resolved ultrafast dynamics in triple degenerate topological semimetal molybdenum phosphide, Acta Phys. Sin. **69**, 077801 (2020).

[26] J. Hasaien, K. J. Zhu, F. Sun, Y. L. Wu, Y. G. Shi, and Jimin Zhao, Generation and control of photo-excited thermal currents in triple degenerate topological semimetal MoP with circularly polarized ultrafast light puleses, Acta Phys. Sin. **69**, 207801 (2020).

[27] Y. L. Wu, X. Yin, J. Hasaien, Y. Ding, and Jimin Zhao, High-pressure ultrafast dynamics in Sr$_2$IrO$_4$: pressure-induced phonon bottleneck effect, Chin. Phys. Lett. (Express Letter) **37**, 047801 (2020).

[28] H. Chu, L. Zhao, A. de la Torre, T. Hogan, S. D. Wilson, and D. Hsieh, A charge density

wave-like instability in a doped spin– orbit-assisted weak Mott insulator, Nat. Mater. **16**, 200 (2017).

[29] L. L. Hu, M. Yang, Y. L. Wu, Q. Wu, H. Zhao, F. Sun, W. Wang, R. He, S. L. He, H. Zhang, R. J. Huang, L. F. Li, Y. G. Shi, and Jimin Zhao, Strong pseudospin-lattice coupling in $Sr_3Ir_2O_7$: Coherent phonon anomaly and negative thermal expansion, Phys. Rev. B **99**, 094307 (2019).

[30] H. Zhao, Q. C. An, X. Ye, B. H. Yu, Q. H. Zhang, F. Sun, Q. Y. Zhang, F. Yang, J. D. Guo, and Jimin Zhao, Second harmonic generation in AB-type $LaTiO_3$/$SrTiO_3$ superlattices, Nano Energy **82**, 105752 (2021).

[31] Y. L. Wu, X. Yin, J. Z. L. Hasaien, Z. Y. Tian, Y. Ding, and Jimin Zhao, On-site in situ high-pressure ultrafast pump–probe spectroscopy instrument, Rev. Sci. Instrum. **92**, 113002 (2021).

[32] R. Wang, J. B. Zhou, X. S. Wang, L. M. Xie, Jimin Zhao, and Xiaohui Qiu, Layer-dependence charge density wave phase transition stiffness in $1T$-TaS_2 nanoflakes evidenced by ultrafast carrier dynamics, Nano Research **14**, 1162 (2021).

[33] Y. L. Wu, Q. Wu, F. Sun, C. Cheng, Sheng Meng, and Jimin Zhao, Emergence of electron coherence and two-color all-optical switching in MoS_2 based on spatial self-phase modulation, Proc. Natl. Acad. Sci. *USA* **112**, 38 (2015).

[34] Y. C. Tian, H. Tian, Y. L. Wu, L. L. Zhu, L. Q. Tao, W. Zhang, Y. Shu, D. Xie, Y. Yang, Z. Y. Wei, X. H. Lu, T. L. Ren, Chih-Kang Shih, and Jimin Zhao, Coherent generation of photo-thermo-acoustic wave from graphene sheets, Scientific Reports **5**, 10582 (2015).

[35] S. F. Ge, X. F. liu, X. F. Qiao, Q. S. Wang, Z. Xu, J. Qiu, P. H. Tan, Jimin Zhao, and Dong Sun, Coherent longitudinal acoustic phonon approaching THz frequency in multilayer molybdenum disulphide, Scientific Reports **4**, 5722 (2014).

[36] R. Wang, T. Wang, Y. Zhou, Y. L. Wu, X. Zhang, X. Y. He, H. L. Peng, Jimin Zhao, and Xiaohui Qiu, Layer-dependent ultrafast dynamics of α-In_2Se_3 nanoflakes, 2D Mater. **6**, 035034 (2019).

[37] Jimin Zhao, A. V. Bragas, D. J. Lockwood, and R. Merlin, Magnon squeezing in an antiferromagnet: reducing the spin noise below the standard quantum limit, Phys. Rev. Lett. **93**, 107203 (2004).

[38] Jimin Zhao, A. V. Bragas, R. Merlin, and D. J. Lockwood, Magnon squeezing in antiferromagnetic MnF_2 and FeF_2, Phys. Rev. B **73**, 184434 (2006).

[39] C. Aku-Leh, J. M. Zhao, R. Merlin, J. Menéndez, and M. Cardona, Long-lived optical phonons in ZnO studied with impulsive stimulated raman scattering, Phys. Rev. B **71**, 205211 (2005).

[40] A. V. Bragas, C. Aku-Leh, C. Costantino, Alka Ingale, J. M. Zhao, and R. Merlin, Ultrafast optical generation of coherent phonons in $CdTe_{1-x}Se_x$ quantum dots, Phys. Rev. B **69**, 205306 (2004).

[41] L. Perfetti, P. A. Loukakos, M. Lisowski, U. Bovensiepen, M. Wolf, H. Berger, S. Biermann, and A. Georges, Femtosecond dynamics of electronic states in the Mott insulator $1T\text{-}TaS_2$ by time resolved photoelectron spectroscopy, New J. Phys. **10**, 053019 (2008).

[42] C.W. Luo, I. H. Wu, P. C. Cheng, J.-Y. Lin, K. H. Wu, T. M. Uen, J.Y. Juang, T. Kobayashi, D. A. Chareev, O. S. Volkova, and A. N. Vasiliev, Quasiparticle dynamics and phonon softening in FeSe superconductors, Phys. Rev. Lett. **108**, 257006 (2012).

[43] V. V. Kabanov, J. Demsar, and D. Mihailovic, Kinetics of a superconductor excited with a femtosecond optical pulse, Phys. Rev. Lett. **95**, 147002 (2005).

[44] Rui Wang, Brian A. Ruzicka, Nardeep Kumar, Matthew Z. Bellus, Hsin-Ying Chiu, and Hui Zhao, Ultrafast and spatially resolved studies of charge carriers in atomically thin molybdenum disulfide, Phys. Rev. B **86**, 045406 (2012).

[45] N. Gedik, J. Orenstein, Ruixing Liang, D. A. Bonn, and W. N. Hardy, Diffusion of nonequilibrium quasi-particles in a cuprate superconductor, Science **300**, 1410 (2003).

[46] J. Buckeridge and D. O. Scanlon, Electronic band structure and optical properties of boron arsenide, Phys. Rev. Mater. **3**, 051601(R) (2019).

[47] A. Rothwarf, and B. N. Taylor, Measurement of recombination lifetimes in superconductors, Phys. Rev. Lett. **19**, 27 (1967).

[48] C. Giannetti, M. Capone, D. Fausti, M. Fabrizio, F. Parmigiani, and D. Mihailovic, Ultrafast optical spectroscopy of strongly correlated materials and high-temperature superconductors: a non-equilibrium approach, Adv. in Phys. **65**, 58-238 (2016).

[49] S. Yue, G. A. Gamage, M. Mohebinia, D. Mayerich, V. Talari, Y. Deng, F. Tian, S. Y. Dai,

H. R. Sun, V. G. Hadjiev, W. Zhang, G. Y. Feng, Jonathan Hu, D. Liu, Z. M. Wang, Z. F. Ren, and J. M. Bao, Photoluminescence mapping and time-domain thermo-photoluminescence for rapid imaging and measurement of thermal conductivity of boron arsenide, Materials Today Physics **13**, 100194 (2020).

[50] Y. M. Dai, J. Bowlan, H. Li, H. Miao, S. F. Wu, W. D. Kong, P. Richard, Y. G. Shi, S. A. Trugman, J. X. Zhu, H. Ding, A. J. Taylor, D. A. Yarotski, and R. P. Prasankumar, Ultrafast carrier dynamics in the large-magnetoresistance material WTe_2, Phys. Rev. B **92**, 161104 (2015).

[51] V. G. Hadjiev, M. N. Iliev, B. Lv, Z. F. Ren, and C. W. Chu, Anomalous vibrational properties of cubic boron arsenide, Phys. Rev. B **89**, 024308 (2014).

[52] R. C. Dynes, Mcmillan's equation and the T_c of superconductors, Solid State Communications **10**, 615 (1972).

[53] P. B. Allen, Neutron spentroscopy of superconductors, Phys. Rev. B **6**, 2577 (1972).

[54] P. B. Allen, and R. C. Dynes, Transition temperature of strong-coupled superconductors reanalyzed, Phys. Rev. B **12**, 905 (1975).

[55] P. B. Allen, and B. Mitrović, *Theory of superconducting T_c*, New York: Academic Press, 1982.

[56] G. Benedek, J. R. Manson, and S. Miret-Arte´s, The electron–phonon coupling constant for single-layer graphene on metal substrates determined from He atom scattering, Phys. Chem. Chem. Phys. **23**, 7575 (2021).

[57] G. Anemone, M. Garnica, M. Zappia, P. C. Aguilar, A. Al Taleb, C. N. Kuo, C. S. Lue, A. Politano, G. Benedek, Amadeo L Vázquez de Parga, R. Miranda, and D. Farías, Experimental determination of surface thermal expansion and electron–phonon coupling constant of $1T$-$PtTe_2$, 2D Mater. **7**, 025007 (2020).

[58] G. Anemone, A. Al Taleb, G. Benedek, A. C. Gomez, and D. Farías, Electron−Phonon Coupling Constant of $2H$-MoS_2(0001) from Helium-Atom Scattering, J. Phys. Chem. C **123**, 3682-3686 (2019).

[59] Gerald D. Mahan, *Many-particle physics*, Kluwer Academic/Plenum Publishers, 2000.

[60] A. A. Balandin, Thermal properties of graphene and nanostructured carbon materials, Nat. Mater. **10**, 569-581 (2011).

[61] D. Sun, Z. K. Wu, C. Divin, X. B. Li, C. Berger, Walt A. de Heer, Phillip N. First, and Theodore B. Norris, Ultrafast relaxation of excited dirac fermions in epitaxial graphene using optical differential transmission spectroscopy, Phys. Rev. Lett. **101**, 157402 (2008).

[62] R. Gatamov, A. Baydin, H. Krzyzanowska, and N. Tolk, Fluence and wavelength dependent ultrafast differential transmission dynamics in graphene, Mater. Res. Express **7**, 095601 (2020).

[63] S. J. Meng, H. Y. Shi, X. D. Sun, and B. Gao, Tuning ultrafast charge carrier dynamics of monolayer graphene using substrates, J. Phys. Chem. C **124**, 38 (2020).

[64] T. Cheng, Z. F. Liu, and Z. R. Liu, High elastic moduli, controllable bandgap and extraordinary carrier mobility in single-layer diamond, J. Mater. Chem. C **8**, 13819 (2020).

[65] S. Reich, A. C. Ferrari, R. Arenal, A. Loiseau, I. Bello, and J. Robertson, Resonant Raman scattering in cubic and hexagonal boron nitride, Phys. Rev. B **71**, 205201 (2005).

[66] Mingda Li, and Gang Chen, Thermal transport for probing quantum materials, MRS Bull. 45, 348-356 (2020).